GEOPHYSICS, VOL. 81, NO. 6 (NOVEMBER-DECEMBER 2016); P. R447–R456, 14 FIGS.
10.1190/GEO2015-0508.1

CrossMark
click for updates

Downloaded 10/03/16 to 138.67.128.82. Redistribution subject to SEG license or copyright; see Terms of Use at http://library.seg.org/

Elastic wavefield tomography with physical model constraints

Yuting Duan[1] and Paul Sava[1]

ABSTRACT

Data-domain elastic wavefield tomography is an effective method for updating multiparameter elastic models that exploits much of the information provided by observed multicomponent data. However, poor illumination of the subsurface by P- and S-waves often prevents reliable updates of the model parameters. Moreover, differences in illumination, amplitude, and wavelength between P- and S-waves can distort the intrinsic physical relationships between the reconstructed model parameters. We have developed a method for elastic isotropic wavefield tomography that explicitly constrains the relationship between P- and S-wave velocities. By incorporating a model constraint term in the objective function, we confine P- and S-velocity updates to a physical area defined by prior information, for example, by laboratory measurements or well logs. We have determined that this physical constraint yields models that are more physically plausible, compared with models obtained using only the data misfit objective function.

INTRODUCTION

Seismic tomography is a commonly used tool for building models of subsurface parameters from recorded seismic data. The various approaches to seismic tomography generally fall into two categories. The first is traveltime tomography, which seeks to match the traveltimes of recorded seismic data with those of synthetic seismic data simulated in a trial model by using ray tracing (Zhu et al., 1992; Zelt et al., 2006; Taillandier et al., 2009) or by solving a wave equation (Woodward, 1992; Schuster and Quintus-Bosz, 1993). However, models computed with traveltime tomography tend to have lower resolution, and may be less accurate when the subsurface contains complicated geologic structures that result in wavefield multipathing. The second category consists of methods for wavefield tomography, which use the amplitude and phase information of recorded seismic data to invert for the subsurface parameter model. Although more expensive than traveltime tomography, wavefield tomography is more effective in recovering model parameters that are sensitive to waveform amplitudes (Tarantola, 1986; Mora, 1988; Pratt, 1999; Prieux et al., 2013), and it has the ability to recover parameters with higher resolution (Bae et al., 2012; McNeely et al., 2012).

However, one issue with wavefield tomography, including full-waveform inversion (FWI) and other similar methods, is that it has nonunique solutions; i.e., multiple models may fit the data equally well. Ivanov et al. (2005) summarize several factors that contribute to nonuniqueness including, for example, insufficient acquisition and the presence of noise in the data. Methods for regularization have been proposed to stabilize the results and reduce the number of possible solutions (Tikhonov and Arsenin, 1977; Sun and Schuster, 1992; Zhou et al., 2002). Regularization is usually defined in the model domain for the purpose of adding prior information to the model. Regularization can be formulated in many different, possibly complementary, ways. Tikhonov and Arsenin (1977) propose a regularization term that encourages smoothness in the computed model. Xiang and Zhang (2014) use an edge-preserving regularization term to preserve sharp interfaces within the model. Asnaashari et al. (2013) use an a priori model to constrain the inversion. These and other examples demonstrate that proper regularization or preconditioning can effectively reduce the number of nonunique solutions and, in many cases, improve the accuracy of the reconstructed models.

Wavefield tomography is well-developed under the acoustic assumption (Tarantola, 1984; Pratt, 1999; Operto et al., 2004; Biondi and Almomin, 2014); however, recorded seismic data include S-waves in addition to P-waves. Because all wave modes contain useful information about the subsurface, elastic wavefield tomography can allow for better characterization of the subsurface (Tarantola, 1986; Pratt, 1990; Guasch et al., 2012; Vigh et al., 2014). Although multiparameter inversion can provide more physical information compared with single-parameter inversion, different parameters in the updated model may not be physically realistic (Plessix, 2006); i.e., inversion might not be able to resolve the model parameters while preserving their intrinsic physical relationships.

Such physical relationships need to be enforced explicitly because they provide constraints on the model parameters that cannot

Manuscript received by the Editor 22 September 2015; revised manuscript received 21 June 2016; published online 28 September 2016.
[1]Colorado School of Mines, Center for Wave Phenomena, Golden, Colorado, USA. E-mail: yduan@mines.edu; psava@mines.edu.
© 2016 Society of Exploration Geophysicists. All rights reserved.

Downloaded 10/03/16 to 138.67.128.82. Redistribution subject to SEG license or copyright; see Terms of Use at http://library.seg.org/

be achieved using data or shaping regularization terms. For example, Baumstein (2013) imposes rock-physics-based constraints on FWI using the projection onto convex sets method, which clips the values of update model parameters or their relationships to be in the desired bounds and then performs a line search within the feasible region. Using this approach, Baumstein (2013) modifies the gradient and the line search without changing the objective function. Physical relationships between model parameters in elastic media can be derived from well logs, seismic data, and laboratory measurements, and they can also be derived based on first-principle physical relationships (Tsuneyama, 2006; Compton and Hale, 2014). Experiments have established the relationship between P- and S-velocities (Castagna et al., 1985; Katahara, 1999; Tsuneyama, 2006); therefore, enforcing a range of constant ratios between the two velocities could guide the model update, thus increasing the robustness of wavefield tomography.

In this paper, we perform wavefield tomography using the isotropic elastic-wave equation, and we invert for the squared velocities of P- and S-waves simultaneously. We propose an objective function for wavefield tomography that constraints the relationship between P- and S-wave velocities. Examples demonstrate that the model constraints enforce appropriate physical relationships between the model parameters.

ELASTIC WAVEFIELD MODELING

We consider the isotropic elastic-wave equation:

$$\ddot{\mathbf{u}} - \alpha\nabla(\nabla\cdot\mathbf{u}) + \beta\nabla\times(\nabla\times\mathbf{u}) = \mathbf{f}, \tag{1}$$

where $\mathbf{u}(e,\mathbf{x},t) = [\,u_x \quad u_y \quad u_z\,]^T$ is the displacement vector and $\mathbf{f}(e,\mathbf{x},t)$ is the source function. The vectors $\mathbf{u}$ and $\mathbf{f}$ are functions of the experiment index e, spatial location $\mathbf{x}$, and time t. Model parameters $\alpha(\mathbf{x}) = (\lambda + 2\mu/\rho)$ and $\beta(\mathbf{x}) = (\mu/\rho)$ are squared P- and S-wave velocities, respectively. Here, λ and μ are the Lamé parameters and ρ is the density. Equation 1 assumes slowly varying Lamé parameters (Lay and Wallace, 1995) and describes a linear relationship between the displacement vector $\mathbf{u}$ and the source function $\mathbf{f}$:

$$\mathbf{L}\mathbf{u} = \mathbf{f}, \tag{2}$$

where matrix $\mathbf{L}$ is the elastic-wave operator corresponding to equation 1, with model parameters α and β, whose adjoint is written as $\mathbf{L}^\top$.

OBJECTIVE FUNCTION

For wavefield tomography, one typically updates a model by minimizing an objective function. We consider an objective function $\mathcal{J}(\mathbf{u}_s,\alpha,\beta)$ consisting of three terms: a data misfit term $\mathcal{J}_D(\mathbf{u}_s,\alpha,\beta)$, a regularization term $\mathcal{J}_M(\alpha,\beta)$ that allows for the use of prior models $\bar{\alpha}(\mathbf{x})$ and $\bar{\beta}(\mathbf{x})$ as well as model shaping, and a model constraint term $\mathcal{J}_C(\alpha,\beta)$ that restricts the relationship between α and β to a feasible region:

$$\mathcal{J}(\mathbf{u}_s,\alpha,\beta) = \mathcal{J}_D(\mathbf{u}_s,\alpha,\beta) + \mathcal{J}_M(\alpha,\beta) + \mathcal{J}_C(\alpha,\beta). \tag{3}$$

We define the data misfit term using the difference between the predicted and observed data:

$$\mathcal{J}_D = \sum_e \frac{1}{2}\|\mathbf{W}_u\mathbf{u}_s - \mathbf{d}_o\|^2, \tag{4}$$

where $\mathbf{d}_o(e,\mathbf{x},t)$ are the observed data recorded at the receiver locations and weights $\mathbf{W}_u(e,\mathbf{x},t)$ restrict the source wavefield $\mathbf{u}_s(e,\mathbf{x},t)$ to the receiver locations.

The regularization term $\mathcal{J}_M$ in the objective function penalizes deviations from prior models $\bar{\alpha}(\mathbf{x})$ and $\bar{\beta}(\mathbf{x})$:

$$\mathcal{J}_M = \frac{1}{2}\|\mathbf{W}_\alpha(\alpha-\bar{\alpha})\|^2 + \frac{1}{2}\|\mathbf{W}_\beta(\beta-\bar{\beta})\|^2, \tag{5}$$

where $\mathbf{W}_\alpha(\mathbf{x})$ and $\mathbf{W}_\beta(\mathbf{x})$ are the model shaping operators, whose inverses are related to the model covariance matrices. Such operators can be either simple space-invariant roughness operators, e.g., a Laplacian filter (Tarantola, 1987), or they can perform image shaping with nonstationary filtering (Hale, 2007; Guitton et al., 2012).

Due to differences in illumination and amplitude between P- and S-modes, models α and β — computed using only the data misfit term — update independently, and this can lead to physically unrealistic solutions. Prieux et al. (2013) explain the differences in illumination and amplitude in terms of offset between PP-, PS-, SP-, and SS-reflections using diffraction patterns. Moreover, the undesired inconsistency in resolution between the recovered P- and S-velocity models is also due to the fact that the seismic wavelength for shear modes is shorter than that of P-modes; therefore, the updated S-velocity model could have higher resolution than the updated P-velocity model. To eliminate the undesired solutions, one can constrain model updates using physical relationships between α and β, for example, using a region defined by an upper boundary $h_u(\alpha,\beta) = 0$ and a lower boundary $h_l(\alpha,\beta) = 0$:

$$h_u > 0, \tag{6}$$

$$h_l > 0. \tag{7}$$

To keep the updated model within these boundaries, we include in the objective function a constraint term $\mathcal{J}_C$ that uses a logarithmic penalty function (Peng et al., 2002; Nocedal and Wright, 2006; Gasso et al., 2009):

$$\mathcal{J}_C = -\eta\sum_{\mathbf{x}}[\log(h_u) + \log(h_l)]. \tag{8}$$

The constraint term $\mathcal{J}_C$ tends to $-\infty$ as h_u or h_l tends to zero, and thus penalizes violations of inequalities 6 and 7. This constraint term mainly contributes to model updating when the updated model approaches the boundaries. The parameter η weighs the constraint term $\mathcal{J}_C$ relative to other terms in the objective function $\mathcal{J}$. Note that the starting model for inversion must fall between the boundaries.

For elastic wavefield tomography, because the relationship of P- and S-velocities is generally linear (Castagna et al., 1985; Zimmer et al., 2002; Rojas et al., 2005), we set the boundaries to be

$$h_u = -\alpha + c_u\beta + b_u = 0, \tag{9}$$

$$h_l = \alpha - c_l\beta - b_l = 0, \tag{10}$$

where the user-defined parameters c_l, c_u, b_l, and b_u characterize the slopes and α-intercepts of the specific boundaries. Notice that parameters c_l, c_u, b_l, and b_u are functions of spatial location $\mathbf{x}$; i.e., these parameters may vary with the spatial location. For example, the ratios of P- and S-velocities for liquid and gas saturations have distinguishable differences (Gregory, 1976; Hamada, 2004). With prior physical information, one could apply proper constraints to liquid and gas

Downloaded 10/03/16 to 138.67.128.82. Redistribution subject to SEG license or copyright; see Terms of Use at http://library.seg.org/

zones. In areas of the model where the relationship between α and β has high uncertainty, one could set a broad physical constraint that allows for more variation between α and β.

OBJECTIVE FUNCTION GRADIENT

We update the model iteratively using a steepest descent method (Lailly, 1983; Tarantola, 1984). For the wavefield tomography problem, one can directly apply the adjoint-state method to compute the gradient (Plessix, 2006):

$$\boldsymbol{\mathcal{F}}_s = \mathbf{L}\mathbf{u}_s - \mathbf{f}_s = \mathbf{0}. \tag{11}$$

Equation 11 indicates that we compute the source wavefield $\mathbf{u}_s$ from a given source function $\mathbf{f}_s$; i.e., $\mathbf{u}_s$ is a solution to the given wave equation.

The gradient of the objective function can be efficiently computed using the adjoint-state method (Plessix, 2006). The augmented functional $\mathcal{H}$ is defined as

$$\mathcal{H} = \mathcal{J} - \sum_e \boldsymbol{\mathcal{F}}^\top \mathbf{a}_s. \tag{12}$$

The gradient of $\mathcal{H}$ indicates the search direction toward the minimum of $\mathcal{J}$, constrained by $\boldsymbol{\mathcal{F}}_s = 0$. The adjoint variable, vector $\mathbf{a}_s(e, \mathbf{x}, t)$, is computed by solving the adjoint equations obtained by setting the partial derivatives of the augmented functional relative to the state variables $\mathbf{u}_s$ to zero:

$$\mathbf{L}^\top \mathbf{a}_s = \mathbf{g}_s, \tag{13}$$

where $\mathbf{g}_s(e, \mathbf{x}, t)$ is the adjoint source given by

$$\mathbf{g}_s = \frac{\partial \mathcal{J}}{\partial \mathbf{u}_s} = \mathbf{W}_u^\top (\mathbf{W}_u \mathbf{u}_s - \mathbf{d}_o). \tag{14}$$

Note that because terms $\mathcal{J}_M$ and $\mathcal{J}_C$ are not functions of $\mathbf{u}_s$, they do not appear in the expression for the adjoint source.

The gradient of the augmented functional $\mathcal{H}$ is given by

$$\begin{bmatrix} \frac{\partial \mathcal{H}}{\partial \alpha} \\ \frac{\partial \mathcal{H}}{\partial \beta} \end{bmatrix} = \begin{bmatrix} \frac{\partial \mathcal{J}}{\partial \alpha} \\ \frac{\partial \mathcal{J}}{\partial \beta} \end{bmatrix} - \sum_e \begin{bmatrix} \frac{\partial \boldsymbol{\mathcal{F}}_s^\top}{\partial \alpha} \mathbf{a}_s \\ \frac{\partial \boldsymbol{\mathcal{F}}_s^\top}{\partial \beta} \mathbf{a}_s \end{bmatrix}. \tag{15}$$

We obtain the gradient of $\mathcal{J}_D$ by solving $(\partial \mathcal{H}/\partial \alpha) = 0$ and $(\partial \mathcal{H}/\partial \beta) = 0$

$$\begin{bmatrix} \frac{\partial \mathcal{J}_D}{\partial \alpha} \\ \frac{\partial \mathcal{J}_D}{\partial \beta} \end{bmatrix} = \sum_e \begin{bmatrix} \frac{\partial \boldsymbol{\mathcal{F}}_s^\top}{\partial \alpha} \mathbf{a}_s \\ \frac{\partial \boldsymbol{\mathcal{F}}_s^\top}{\partial \beta} \mathbf{a}_s \end{bmatrix} = \sum_e \begin{bmatrix} -[\nabla(\nabla \cdot \mathbf{u}_s)]^\top \star \mathbf{a}_s \\ [\nabla \times (\nabla \times \mathbf{u}_s)]^\top \star \mathbf{a}_s \end{bmatrix}, \tag{16}$$

where the symbol $\star$ denotes zero-lag crosscorrelation. In addition, we apply illumination compensation to the gradient for the data misfit term, by dividing the gradient with respect to α by $\sum_t [\nabla(\nabla \cdot \mathbf{u}_s)]^2$ and the gradient with respect to β by $\sum_t [\nabla \times (\nabla \times \mathbf{u}_s)]^2$. This compensation is an approximation for the diagonal of the inverse Hessian (Pratt et al., 1998).

The gradient of terms $\mathcal{J}_M$ and $\mathcal{J}_C$, with respect to the model parameters α and β, are

$$\begin{bmatrix} \frac{\partial \mathcal{J}_M}{\partial \alpha} \\ \frac{\partial \mathcal{J}_M}{\partial \beta} \end{bmatrix} = \begin{bmatrix} \mathbf{W}_\alpha^\top \mathbf{W}_\alpha (\alpha - \bar{\alpha}) \\ \mathbf{W}_\beta^\top \mathbf{W}_\beta (\beta - \bar{\beta}) \end{bmatrix}, \tag{17}$$

and

$$\begin{bmatrix} \frac{\partial \mathcal{J}_C}{\partial \alpha} \\ \frac{\partial \mathcal{J}_C}{\partial \beta} \end{bmatrix} = \begin{bmatrix} \frac{-\eta}{\alpha - c_u\beta - b_u} - \frac{\eta}{\alpha - c_l\beta - b_l} \\ \frac{\eta c_u}{\alpha - c_u\beta - b_u} + \frac{\eta c_l}{\alpha - c_l\beta - b_l} \end{bmatrix}, \tag{18}$$

respectively. When updated models approach the boundaries defined in $\mathcal{J}_C$, the gradient of $\mathcal{J}_C$ dominates the total gradient of the objective function $\mathcal{J}$, thus pushing the updated model away from the boundaries. When the updated models are distant from the boundaries defined in $\mathcal{J}_C$, the gradient of $\mathcal{J}_C$ has less influence on the total gradient $\mathcal{J}$, and the data misfit term controls the inversion.

We update the model using a steepest-descent method in which we search for the step length via a quadratic line search in the direction opposite of the gradient of the objective function. This line search requires at least two additional evaluations of the objective function. In addition, when using logarithmic functions in the physical constraint term, one must ensure that the model remains in the predefined feasible region while performing the line search and model update.

EXAMPLE

We illustrate our method for elastic wavefield tomography with two synthetic models and compare inversion using only the data misfit term $\mathcal{J}_D$ with inversion using the data misfit with physical constraints $\mathcal{J}_D + \mathcal{J}_C$.

Borehole model

The first-synthetic model contains two negative Gaussian anomalies centered at (1.5, 2.0) and (1.5, 5.0) km. There are 60 vertical displacement sources in a well at $x = 0.2$ km and a line of geophones at $x = 2.8$ km. The α and β models are shown in Figure 1. The vertical component of a shot gather is shown in Figure 2a, which contains P- and S-waves. To illustrate the influence of the physical constraint term $\mathcal{J}_C$ when the illumination of P- and

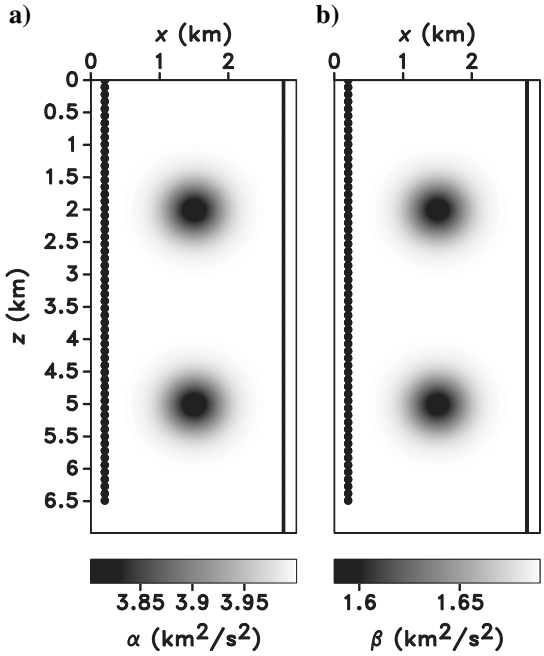


Figure 1. The (a) α and (b) β models with two negative Gaussian anomalies. Dots are the source locations at $x = 0.2$ km, and the vertical line shows the receivers at $x = 2.8$ km.

Downloaded 10/03/16 to 138.67.128.82. Redistribution subject to SEG license or copyright; see Terms of Use at http://library.seg.org/

S-waves differ, we mute the S-waves in the observed and predicted data for receivers located between $z = 0$ and 3.5 km, and the P-waves in the observed and predicted data for receivers located between $z = 3.5$ and 7 km, as shown in Figure 2b. That is, for elastic wavefield tomography, we use primarily the P-waves passing through the shallow Gaussian anomaly and the S-waves passing through the deeper Gaussian anomaly. This is simply an artificial construction meant to simulate partial illumination and to highlight the influence of the model constraint.

Using the data misfit term $\mathcal{J}_D$ as the objective function, we obtain the updated models for α and β after 21 iterations, shown in Figures 3a and 4a, respectively. Notice that the model update of α focuses on the shallow Gaussian anomaly, whereas that of β focuses on the deeper Gaussian anomaly. By including the physical constraint term $\mathcal{J}_C$ in the objective function, we obtain the updated α and β models shown in Figures 3b and 4b, respectively. We choose the weighting parameter η to be 0.6 to balance the gradients of $\mathcal{J}_D$ and $\mathcal{J}_C$. Observe that the Gaussian anomalies in α and β recovered using physical constraints (Figures 3b and 4b) are more accurate compared with those obtained without constraints (Figures 3a and 4a). Figure 5a and 5b shows, respectively, the values of the updated

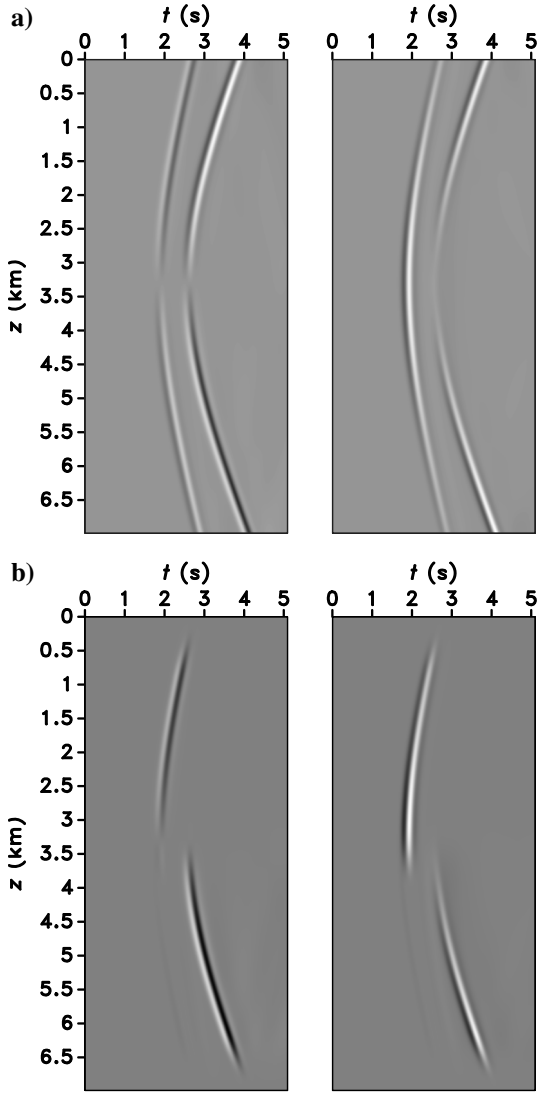


Figure 2. Horizontal (left panels) and vertical (right panels) components of a shot gather with the source at $z = 3.5$ km. The first arrival is the P-wave, and the second arrival is the S-wave. (a) The original data. (b) Processed data for inversion with P-waves only from $z = 0$ to 3.5 km and S-waves only from $z = 3.5$ to 7 km. We window selected portions of the original data to simulate partial illumination for different wave modes.

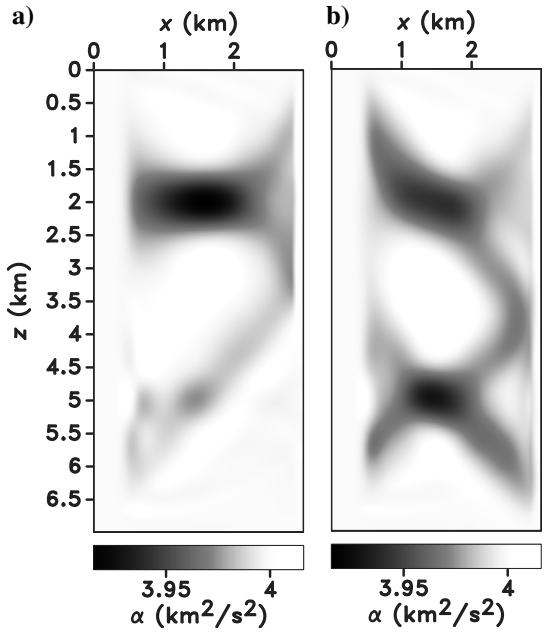


Figure 3. Updated α models after 21 iterations using (a) objective function $\mathcal{J}_D$ and (b) $\mathcal{J}_D + \mathcal{J}_C$. Note that the Gaussian anomaly in (b) at (1.5, 5) km is better recovered, and its amplitude and shape are closer to the true model compared with that in (a).

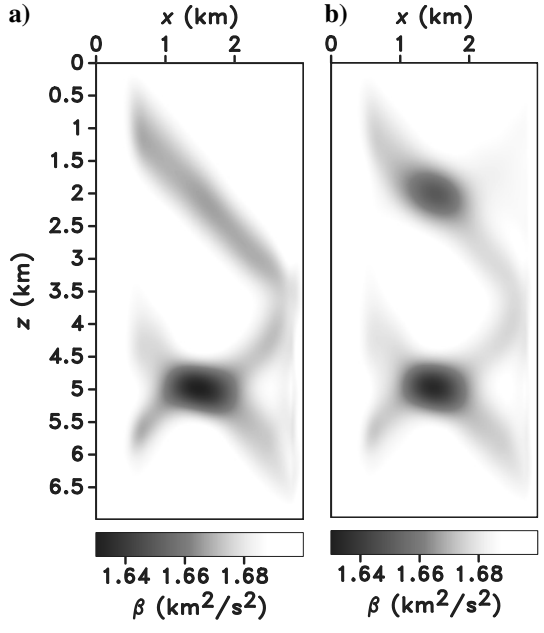


Figure 4. Updated β models after 21 iterations using (a) objective function $\mathcal{J}_D$ and (b) $\mathcal{J}_D + \mathcal{J}_C$. Note that the Gaussian anomaly in (b) at (1.5, 2) km is better recovered, and its amplitude and shape are closer to the true model compared with that in (a).

Downloaded 10/03/16 to 138.67.128.82. Redistribution subject to SEG license or copyright; see Terms of Use at http://library.seg.org/

models at (1.5, 2) and (1.5, 5) km as a function of the iteration number. In both figures, the stars represent the updated models with constraints, whereas the dots represent the updated models without constraints. Notice in Figure 5a that the recovered α and β models tend to move toward the lower constraint boundary in later iterations. In contrast, by including the physical constraint term $\mathcal{J}_C$ in the objective function, we preserve the ratio between α and β.

Marmousi model

The second example, shown in Figure 6a and 6b, uses a modified Marmousi model (Versteeg, 1991, 1993). The top layer from 0 to 110 m is elastic and homogeneous. For this synthetic example, we assume that we know the values of α and β for the first layer. Figure 6c shows the crossplot of α and β measured from three well logs at $x = 1.0$, 2.0, and 3.0 km. The relationship between α and β in the well logs is approximately linear; therefore, we use two straight lines (equations 9 and 10) to define the feasible region for the α-β relationships, which provides the prior physical constraints for inversion.

The starting α and β models (shown in Figure 7a and 7b, respectively) are computed by smoothing the true model mainly along the horizontal axis. Note that in the crossplot of a and b models shown in Figure 7c, all samples in the model space are within the predefined feasible range. We simulate 20 shots using displacement sources evenly distributed along the x-axis, at depth $z = 0.04$ km, and record each shot with 500 receivers evenly distributed along the x-axis, at depth $z = 0.07$ km. The amplitude of the horizontal component of the displacement source is five times stronger than the vertical component, so that the computed wavefields contain strong S-waves. The FWI is carried out using a multiscale approach with two frequency bands: 0–5 and 0–7 Hz. The horizontal and vertical components of the data residual for the first frequency band, computed using the starting model, are shown in Figure 8a and 8b, respectively. Notice that the data residual contains head waves, diving waves, and reflections.

We perform four different tests using the same starting models shown in Figure 7a and 7b to evaluate the constraint term $\mathcal{J}_C$. For the first test, we use only the data misfit term $\mathcal{J}_D$ as the objective function. Figure 8a and 8b shows, respectively, the horizontal and vertical components of the data residual for the first frequency band before inversion. In comparison, Figure 8c and 8d shows the data residual after inversion using only the first frequency band. The final model for the first frequency band is then used as the starting model for the second frequency band. The data residual for the second frequency band before inversion is shown in Figure 9a and 9b, whereas Figure 9c and 9d shows the data residual after inversion using the same frequency band. As expected, the magnitude of the data residual, in which we observe energy from all wave types, has decreased after inversion.

Figure 10a and 10b shows the recovered α and β models after inversion using both frequency bands. Notice that the recovered β contains more structural details, for example, in the high-velocity zones,

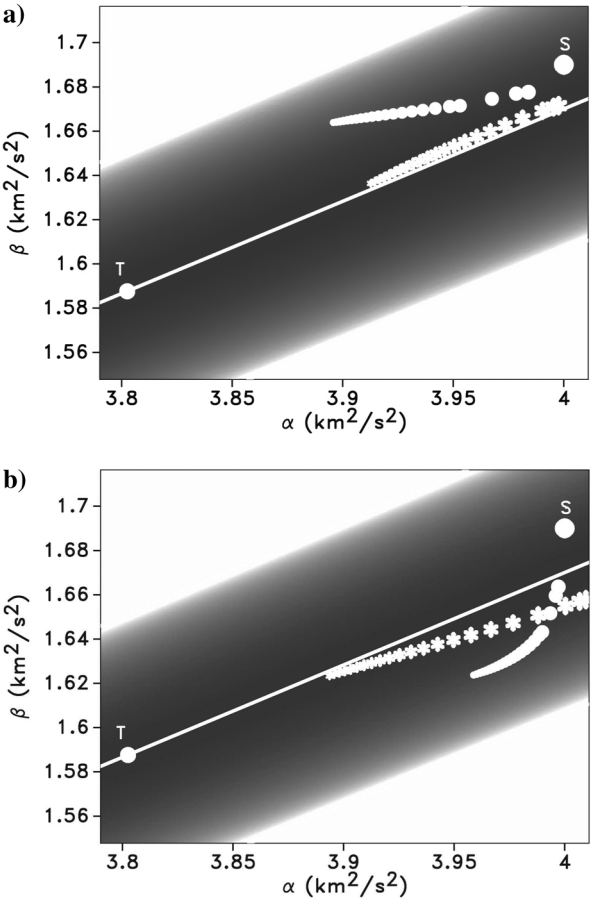


Figure 5. Model updates for the Gaussian model in Figure 1 as a function of iterations at (a) (1.5, 2) km and (b) (1.5, 5) km. Stars and dots are the updated models with and without constraints, respectively. Note that without constraints, the α and β models update toward the boundaries, whereas with constraints, the relationship of α and β models is enforced to be close to the true model indicated by the median line in the underlying physical constraint.

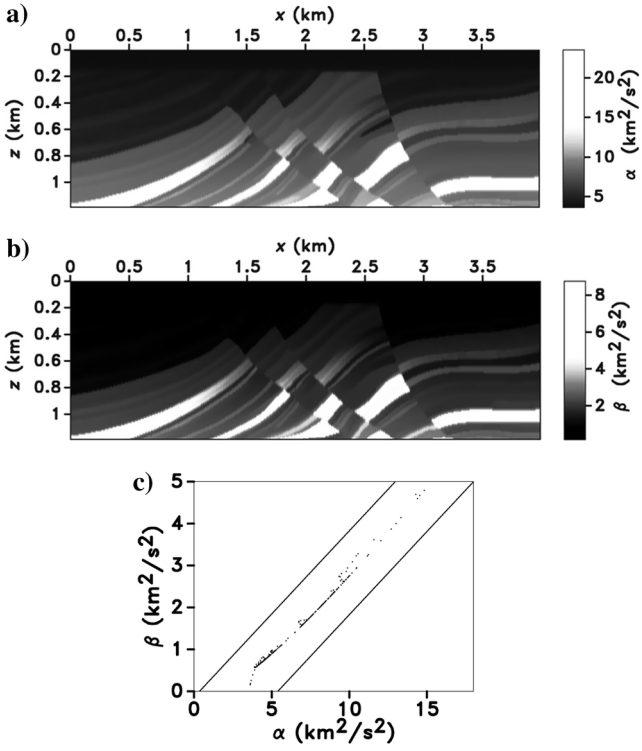


Figure 6. (a) True α model, (b) true β model, and (c) the crossplot of α and β models. The α and β models are computed from the original Marmousi P- and S-velocity models, respectively.

Downloaded 10/03/16 to 138.67.128.82. Redistribution subject to SEG license or copyright; see Terms of Use at http://library.seg.org/

whereas the recovered α model is smoother. The recovered α and β values are crossplotted in Figure 10c. Without physical constraints, the α and β values deviate from the allowable region, resulting in recovered models that are inaccurate. One reason for the difference between the recovered α and β models is that the wavelengths of P- and S-waves differ significantly. Because there is no attenuation in this synthetic example, typical S-wavelengths are shorter than P-wavelengths for the same frequency band. This results in the recovered β model having higher resolution than the α model, as shown in Figure 10. In reality, however, S-waves experience more attenuation than P-waves for the same frequency band, and the resolution of the recovered α and β models still differ in practice. This inconsistency in resolution between the recovered α and β models does not reflect the true subsurface, and we address this inconsistency through physical constraints between the two model parameters.

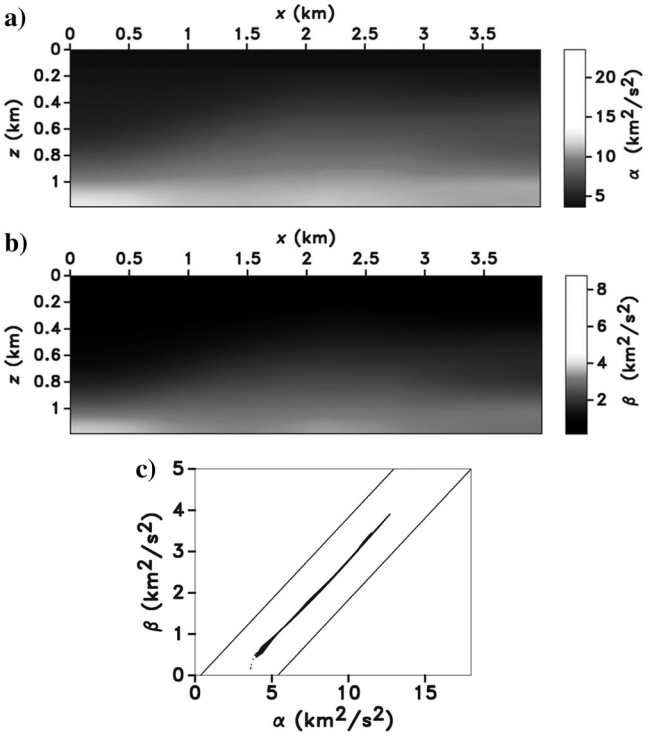


Figure 7. (a) Starting α model, (b) starting β model, and (c) crossplot of α and β models for Marmousi example. The α and β models are computed from the true model with smoothing mainly along the horizontal axis to eliminate detailed structures in the true model.

For the remaining tests, we include the data misfit term $\mathcal{J}_D$ and the physical constraint term $\mathcal{J}_C$ in the objective function. For the second test, we use upper and lower boundaries estimated from the three well logs as shown in Figure 6c. By including the physical constraint term in the objective function, the values of α and β are confined to the allowable range. Figure 11a and 11b shows the updated α and β models after the inversion converges. Compared with the models obtained using only the data misfit term (Figure 10), both models shown in Figure 11 now have similar resolution. Figure 11c shows the crossplot of the recovered α and β models, and confirms that the α-β relationship is maintained within the allowable region as the models are updated. For this test and the following tests, the weighting parameter we use in the constraint term is $\eta = 4.0$.

For the third test, we increase the width of the feasible region, as indicated by the solid lines in the crossplot in Figure 12c. The α and β models obtained with these less-restrictive constraints are shown in Figure 12a and 12b. Compared with the second test (Figure 11), the recovered α and β models exhibit larger differences in resolution and, as evidenced by the crossplot in Figure 12c, more variation in the ratio between the values of α and β.

For the last test, we purposely select a feasible region, shown in Figure 13c, whose center does not coincide with the best-fit line describing the relationship between α and β derived from the three

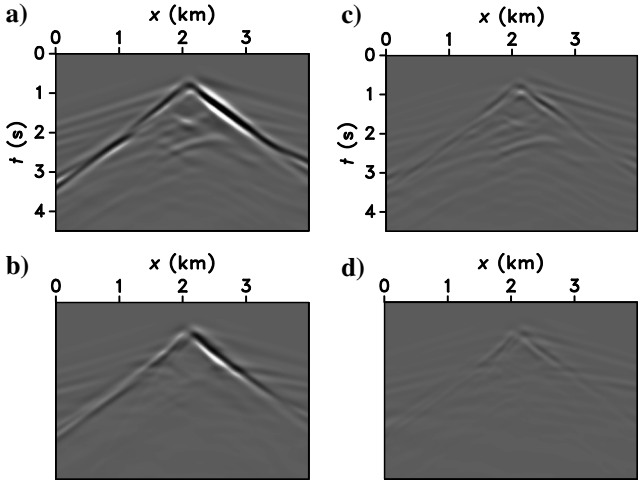


Figure 8. (a) Vertical and (b) horizontal components of the difference between a recorded shot gather and the corresponding predicted data for the first frequency band (0–5 Hz). The predicted data are computed using the initial model shown in Figure 7a and 7b; (c) vertical and (d) horizontal components of the difference between the recorded and predicted data for the first frequency band. The predicted data are computed using the final model for the first frequency band.

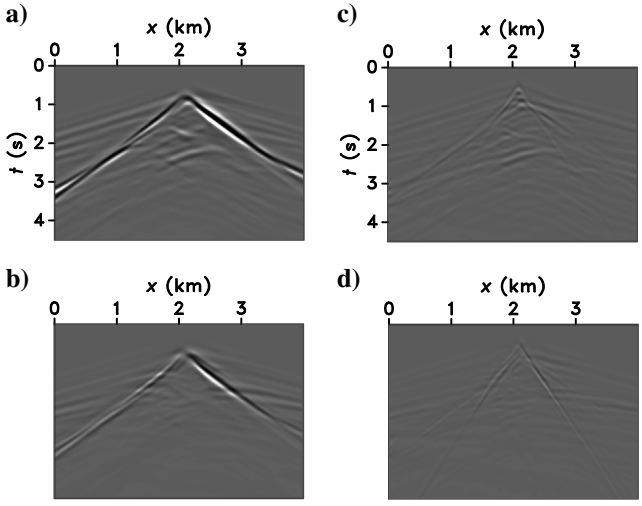


Figure 9. (a) Vertical and (b) horizontal components of the difference between a recorded shot gather and the corresponding predicted data for the second frequency band (0–7 Hz). The predicted data are computed using the final model from the first frequency band; (c) vertical and (d) horizontal components of the difference between the recorded and predicted data for the second frequency band. The predicted data are computed using the final model for the second frequency band.

Downloaded 10/03/16 to 138.67.128.82. Redistribution subject to SEG license or copyright; see Terms of Use at http://library.seg.org/

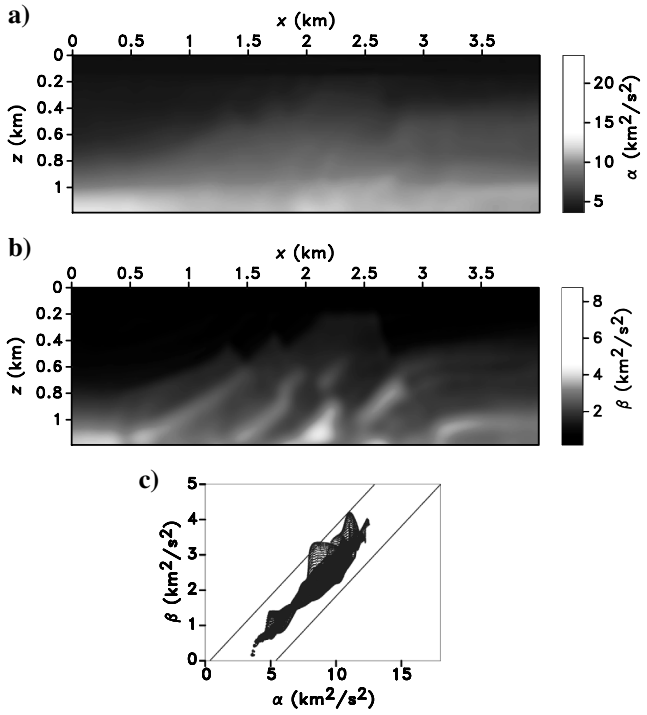


Figure 10. Recovered (a) α and (b) β models after the inversion of the second frequency band. (c) Crossplot of the recovered α and β models using objective function $\mathcal{J}_D$. Note that the recovered β model contains more details than the α model.

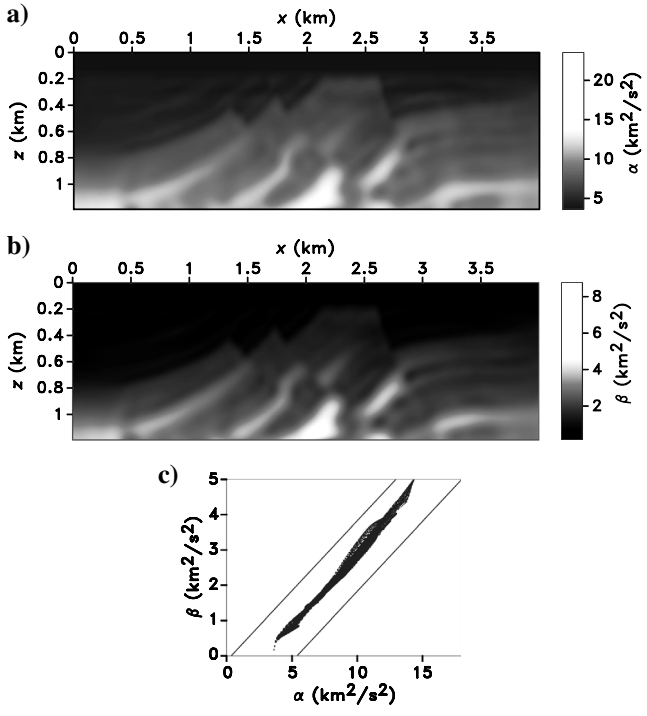


Figure 11. Recovered (a) α and (b) β models after the inversion of the second frequency band. (c) Crossplot of the recovered α and β models using objective function $\mathcal{J}_D + \mathcal{J}_C$. The upper and lower boundaries are indicated by the two solid lines. Note that the recovered α and β models contain similar details.

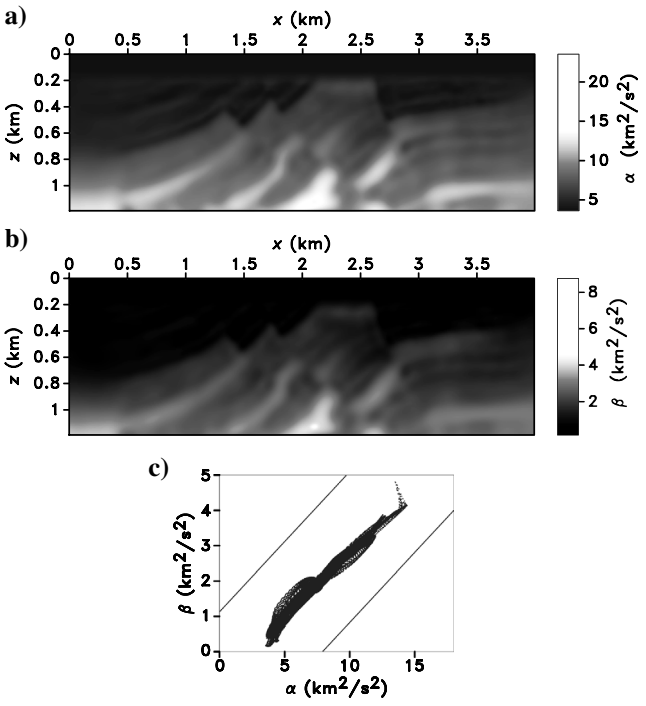


Figure 12. Recovered (a) α and (b) β models after the inversion of the second frequency band. (c) Crossplot of the recovered α and β models using objective function $\mathcal{J}_D + \mathcal{J}_C$. This feasible region is broader than the original region.

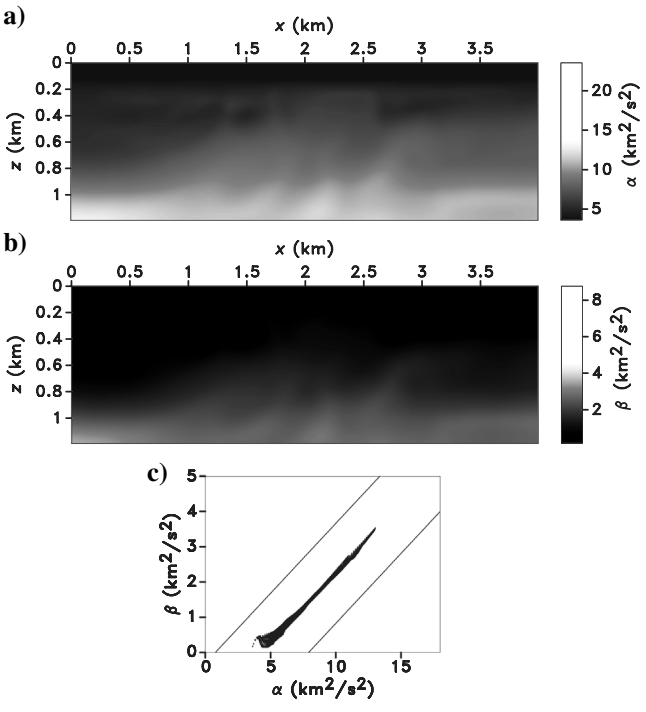


Figure 13. Recovered (a) α and (b) β models after the inversion of the second frequency band. (c) Crossplot of the recovered α and β models using objective function $\mathcal{J}_D + \mathcal{J}_C$. The center of the feasible region does not coincide with the best-fit line describing the relationship between α and β.

Downloaded 10/03/16 to 138.67.128.82. Redistribution subject to SEG license or copyright; see Terms of Use at http://library.seg.org/

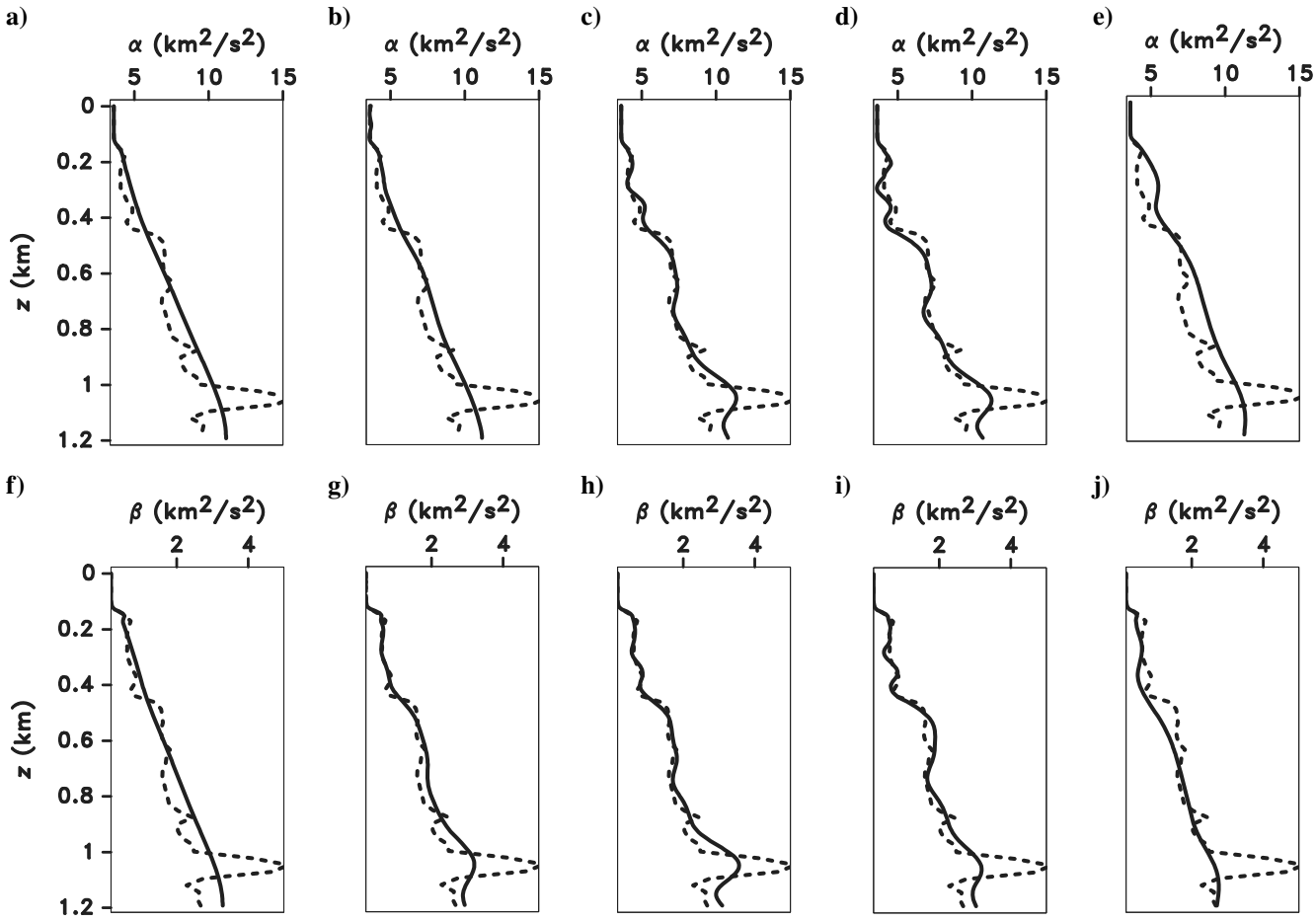


Figure 14. Comparison between initial or recovered models (solid lines) and true models (dashed lines) from the well at $x = 2.4$ km. Row one: Solid lines are the α profiles of (a) initial model; (b) updated models using objective function $\mathcal{J}_D$; (c) updated models using objective function $\mathcal{J}_D + \mathcal{J}_C$; (d) updated models using objective function $\mathcal{J}_D + \mathcal{J}_C$, where $\mathcal{J}_C$ is defined with a wider feasible region; (e) updated models using objective function $\mathcal{J}_D + \mathcal{J}_C$, where $\mathcal{J}_C$ is defined with a shifted feasible region. Row two: Solid lines are the β profiles of (f) initial model; (g) updated models using objective function $\mathcal{J}_D$; (h) updated models using objective function $\mathcal{J}_D + \mathcal{J}_C$; (i) updated models using objective function $\mathcal{J}_D + \mathcal{J}_C$, where $\mathcal{J}_C$ is defined with a wider feasible region; (j) updated models using objective function $\mathcal{J}_D + \mathcal{J}_C$, where $\mathcal{J}_C$ is defined with a shifted feasible region. In panels (c, d, g, h, and i), the recovered model profiles match the true models.

well logs. Using this constraint, the recovered α (Figure 13a) and β models (Figure 13b) are much smoother compared with those from the second (Figure 11) and third (Figure 12) tests. In this case, because the constraint term drives the relation between α and β toward incorrect values, neither the α nor β models are updated correctly. Therefore, from the results of this test and the previous tests, we conclude that ideally one should choose a narrow constraint region that enforces an accurate relation between α and β but, when there is significant uncertainty in the estimated relation between α and β, choosing a broader constraint region is a preferable alternative to choosing a narrow constraint region that enforces an inaccurate relationship.

Vertical profiles extracted from α and β models at $x = 2.0$ km are shown in Figure 14. The solid line in Figure 14a is the initial α model, whereas the solid lines in Figure 14b–14e are the recovered α models from the four tests. The dashed line in Figure 14a–14e indicates the true α model. Similarly, the solid line in Figure 14f is the initial β model, the solid lines in Figure 14g–14j are the recovered β models from the four tests, and the dashed line in Figure 14f–14j is the true β model. Using only the data misfit as the objective function, we obtain a reliable model update for β (Figure 14b), but only a limited model update for α (Figure 14g). When using constraints that enforce an accurate relationship between α and β, which are estimated from the three well logs, we obtain updated α and β models that match the true model well. The recovered α (Figure 14c) and β (Figure 14h) models obtained with narrower constraints (Figure 11) are slightly more accurate than the α (Figure 14d) and β (Figure 14i) models obtained with broader constraints (Figure 12). Using narrow but inaccurate constraints (Figure 13) yields unsatisfactory results for α (Figure 14e) and β (Figure 14j).

CONCLUSIONS

We demonstrate an elastic wavefield tomography method based on the isotropic elastic wave equation, formulated to reduce the misfit between the observed and predicted data, and constrained to obtain models that are physically plausible. We invert for a model of multiple elastic material parameters, specifically the squared velocities of P- and S-waves. Due to differences in illumination, ampli-

Downloaded 10/03/16 to 138.67.128.82. Redistribution subject to SEG license or copyright; see Terms of Use at http://library.seg.org/

tude, and wavelength between P- and S-waves, the model updates for the two parameters may differ in amplitude and location, thus leading to nonphysical models. To obtain a physically realistic model, we introduce physical constraints that force the updated models to satisfy known physical relations bounded within a certain feasible range. This constraint term only impacts model updating, when the inverted model parameters are close to the boundaries of the constraints.

For multiparameter wavefield tomography in general, another issue is the trade-off between model parameters, particularly in cases where data coverage is incomplete. The choice of model parameterization is an important aspect of multiparameter wavefield tomography, and different parameterizations have been investigated to determine optimal combinations for inversion that result in minimal ambiguity between parameters. However, in general, this ambiguity cannot be completely avoided even with an optima parameterization. By including a physical constraint term in the objective function, we limit the set of permissible solutions, and thereby we can potentially reduce the trade-off between parameters, and, more generally, the nonlinearity of the inverse problem. For example, we could use our knowledge of the fact that the P-wave velocity must be greater than S-wave velocity to constrain the inversion to yield only solutions that meet this criteria.

The use of a model constraint that links the model updates for multiparameters could also be applied to other wavefield tomography problems. For example, for acoustic wavefield tomography, in which one inverts for P-wave velocity and impedance, one could constrain the relationship between these two parameters to lie within a physically plausible range. In addition, without imposing a hard relation between velocity and density, one could define arbitrary bounds on the feasible region, for example, by using experimental probability density functions established between the model parameters based on well log or other information.

ACKNOWLEDGMENTS

We thank the sponsor companies of the Center for Wave Phenomena, whose support made this research possible. The reproducible numeric examples in this paper use the Madagascar open-source software package (Fomel et al., 2013) freely available from http://www.ahay.org.

REFERENCES

Asnaashari, A., R. Brossier, S. Garambois, F. Audebert, P. Thore, and J. Virieux, 2013, Regularized seismic full waveform inversion with prior model information: Geophysics, **78**, no. 2, R25–R36, doi: 10.1190/geo2012-0104.1.

Bae, H. S., S. Pyun, C. Shin, K. J. Marfurt, and W. Chung, 2012, Laplace-domain waveform inversion versus refraction-traveltime tomography: Geophysical Journal International, **190**, 595–606, doi: 10.1111/j.1365-246X.2012.05504.x.

Baumstein, A., 2013, POCS-based geophysical constraints in multi-parameter full wavefield inversion: Presented at the 75th EAGE Conference and Exhibition, incorporating SPE EUROPEC 2013.

Biondi, B., and A. Almomin, 2014, Efficient and robust waveform-inversion workflow: 84th Annual International Meeting, SEG, Expanded Abstracts, 917–921.

Castagna, J. P., M. L. Batzle, and R. L. Eastwood, 1985, Relationships between compressional-wave and shear-wave velocities in elastic silicate rocks: Geophysics, **50**, 571–581, doi: 10.1190/1.1441933.

Compton, S., and D. Hale, 2014, Estimating V_P/V_S ratios using smooth dynamic image warping: Geophysics, **79**, no. 6, V201–V215, doi: 10.1190/geo2014-0022.1.

Fomel, S., P. Sava, I. Vlad, Y. Liu, and V. Bashkardin, 2013, Madagascar: Open-source software project for multidimensional data analysis and reproducible computational experiments: Journal of Open Research Software, **1**, e8, doi: 10.5334/jors.ag.

Gasso, G., A. Rakotomamonjy, and S. Canu, 2009, Recovering sparse signals with a certain family of non-convex penalties and DC programming: IEEE Transactions on Signal Processing, **57**, 4686–4698, doi: 10.1109/TSP.2009.2026004.

Gregory, A., 1976, Fluid saturation effects on dynamic elastic properties of sedimentary rocks: Geophysics, **41**, 895–921, doi: 10.1190/1.1440671.

Guasch, L., M. Warner, T. Nangoo, J. Morgan, A. Umpleby, I. Stekl, and N. Shah, 2012, Elastic 3D full-waveform inversion: 82nd Annual International Meeting, SEG, Expanded Abstracts, doi: 10.1190/segam2012-1239.1.

Guitton, A., G. Ayeni, and E. Daz, 2012, Constrained full-waveform inversion by model reparameterization: Geophysics, **77**, no. 2, R117–R127, doi: 10.1190/geo2011-0196.1.

Hale, D., 2007, Local dip filtering with directional Laplacians: CWP Consortium Project on Seismic Inverse Methods for Complex Structures, 91–102.

Hamada, G., 2004, Reservoir fluids identification using V_P/V_S ratio: Oil & Gas Science and Technology, **59**, 649–654, doi: 10.2516/ogst:2004046.

Ivanov, J., R. D. Miller, J. Xia, D. Steeples, and C. B. Park, 2005, The inverse problem of refraction travel times. Part I: Types of geophysical nonuniqueness through minimization: Pure and Applied Geophysics, **162**, 447–459, doi: 10.1007/s00024-004-2615-1.

Katahara, K. W., 1999, Effect of mineral V_P/V_S on rock V_P/V_S: 69th Annual International Meeting, SEG, Expanded Abstracts, 1029–1032.

Lailly, P., 1983, The seismic inverse problem as a sequence of before stack migrations: Conference on Inverse Scattering: Theory and Application, SIAM, Expanded Abstracts, 206–220.

Lay, T., and T. Wallace, 1995, Modern global seismology: Academic Press.

McNeely, J., T. Keho, T. Tonellot, R. Ley, and J. Chen, 2012, 3D acoustic waveform inversion of land data: A case study from Saudi Arabia: 82nd Annual International Meeting, SEG, Expanded Abstracts, doi: 10.1190/segam2012-0150.1.

Mora, P., 1988, Inversion of seismic wavefield data for P- and S-wave velocity: Exploration Geophysics, **19**, 312–316, doi: 10.1071/EG988312.

Nocedal, J., and S. J. Wright, 2006, Numerical optimization: Springer.

Operto, S., C. Ravaut, L. Improta, J. Virieux, A. Herrero, and P. Dell'Aversana, 2004, Quantitative imaging of complex structures from dense wide-aperture seismic data by multiscale traveltime and waveform inversions: A case study: Geophysical Prospecting, **52**, 625–651, doi: 10.1111/j.1365-2478.2004.00452.x.

Peng, J., C. Roos, and T. Terlaky, 2002, Self-regular functions and new search directions for linear and semidefinite optimization: Mathematical Programming, **93**, 129–171, doi: 10.1007/s101070200296.

Plessix, R. E., 2006, A review of the adjoint-state method for computing the gradient of a functional with geophysical applications: Geophysics Journal International, **167**, 495–503, doi: 10.1111/j.1365-246X.2006.02978.x.

Pratt, R. G., 1990, Inverse theory applied to multi-source cross-hole tomography: Geophysical Prospecting, **38**, 311–329, doi: 10.1111/j.1365-2478.1990.tb01847.x.

Pratt, R. G., 1999, Seismic waveform inversion in the frequency domain. Part 1: Theory and verification in a physical scale model: Geophysics, **64**, 888–901, doi: 10.1190/1.1444597.

Pratt, R. G., C. Shin, and G. Hick, 1998, Gauss-Newton and full Newton methods in frequency-space seismic waveform inversion: Geophysical Journal International, **133**, 341–362, doi: 10.1046/j.1365-246X.1998.00498.x.

Prieux, V., R. Brossier, S. Operto, and J. Virieux, 2013, Multiparameter full waveform inversion of multicomponent ocean-bottom-cable data from the Valhall field. Part 2: Imaging compressive-wave and shear-wave velocities: Geophysical Journal International, **194**, 1665–1681, doi: 10.1093/gji/ggt178.

Rojas, E., T. L. Davis, M. Batzle, M. Prasad, and R. J. Michelena, 2005, V_P/V_S ratio sensitivity to pressure, fluid, and lithology changes in tight gas sandstones: 75th Annual International Meeting, SEG, Expanded Abstracts, 1401–1404.

Schuster, G. T., and A. Quintus-Bosz, 1993, Wavepath eikonal traveltime inversion: Theory: Geophysics, **58**, 1314–1323, doi: 10.1190/1.1443514.

Sun, Y., and G. Schuster, 1992, Hierarchic optimizations for smoothing and cooperative inversion: 62nd Annual International Meeting, SEG, Expanded Abstracts, 745–748.

Taillandier, C., M. Noble, H. Chauris, and H. Calandra, 2009, First-arrival traveltime tomography based on the adjoint-state method: Geophysics, **74**, no. 6, WCB1–WCB10, doi: 10.1190/1.3250266.

Tarantola, A., 1984, Inversion of seismic reflection data in the acoustic approximation: Geophysics, **49**, 1259–1266, doi: 10.1190/1.1441754.

Tarantola, A., 1986, A strategy for nonlinear elastic inversion of seismic reflection data: Geophysics, **51**, 1893–1903, doi: 10.1190/1.1442046.

Tarantola, A., 1987, Inverse problem theory: Methods for data fitting and model parameter estimation: Elsevier Science Publishing Company Inc.

Tikhonov, A., and V. Arsenin, 1977, Solution of ill-posed problems: Winston & Sons.

Tsuneyama, F., 2006, Exploring V_P/V_S relations: Approach from effective medium theories: Proceedings of the 8th SEGJ International Symposium, 1–6.

Versteeg, R., 1991, Analysis of the problem of the velocity model determination for seismic imaging: Ph.D. thesis, University of Paris VII.

Versteeg, R., 1993, Sensitivity of prestack depth migration to the velocity model: Geophysics, **58**, 873–882, doi: 10.1190/1.1443471.

Vigh, D., K. Jiao, D. Watts, and D. Sun, 2014, Elastic full-waveform inversion application using multicomponent measurements of seismic data collection: Geophysics, **79**, no. 2, R63–R77, doi: 10.1190/geo2013-0055.1.

Woodward, M. J., 1992, Wave-equation tomography: Geophysics, **57**, 15–26, doi: 10.1190/1.1443179.

Xiang, S., and H. Zhang, 2014, A new adaptive edge-preserving regularization scheme for seismic full waveform inversion: 84th Annual International Meeting, SEG, Expanded Abstracts, 1238–1242.

Zelt, C. A., A. Azaria, and A. Levander, 2006, 3D seismic refraction traveltime tomography at a groundwater contamination site: Geophysics, **71**, no. 5, H67–H78, doi: 10.1190/1.2258094.

Zhou, H., Y. Zhang, and S. Gray, 2002, Regularization algorithms for seismic inverse problems: 72nd Annual International Meeting, SEG, Expanded Abstracts, 942–945.

Zhu, X., D. P. Sixta, and B. G. Angstman, 1992, Tomostatics: Turning-ray tomography + statics corrections: The Leading Edge, **11**, 15–23, doi: 10.1190/1.1436864.

Zimmer, M., M. Prasad, and G. Mavko, 2002, Pressure and porosity influences on V_P/V_S ratio in unconsolidated sands: The Leading Edge, **21**, 178–183, doi: 10.1190/1.1452609.

Downloaded 10/03/16 to 138.67.128.82. Redistribution subject to SEG license or copyright; see Terms of Use at http://library.seg.org/